ADVANCED QUANTUM TECHNOLOGIES
www.advquantumtech.com

Structure, Magnetotransport, and Theoretical Study on the Layered Antiferromagnet Topological Phase $EuCd_2As_2$ under High Pressure

Zhenhai Yu, Xuejiao Chen, Wei Xia, Ningning Wang, Xiaodong Lv, Desheng Wu, Wei Wu, Ziyi Liu, Jinggeng Zhao, Mingtao Li, Shujia Li, Xin Li, Zhaohui Dong, Chunyin Zhou, Lili Zhang, Xia Wang, Na Yu, Zhiqiang Zou, Jianlin Luo, Jinguang Cheng, Lin Wang, Zhicheng Zhong,* and Yanfeng Guo**

Rich nontrivial topological phases rooted in the interplay between magnetism and topology in the layered antiferromagnet $EuCd_2As_2$ have captured vast attention, especially the ideal Weyl semimetal state realized in the spin-polarized ferromagnetic (FM) structure driven by a moderate external magnetic field. In this work, combining magnetization, magneto-transport, and structure measurements under high pressure and first principles calculations, this study finds that the pressure can drive the in-plane antiferromagnetic structure of $EuCd_2As_2$ across an intermediate in-plane FM structure then into the out-of-plane FM structure. This study also finds butterfly-shaped MR and anomalous Hall effect under large pressure, which may support the pressure-driven FM state. High-pressure angle-dispersive X-ray diffraction and X-ray absorption near-edge spectroscopy measurements exclude structure transition and/or change of Eu^{2+} valence state as sources for the magnetic phase transitions. Alternatively, apparently reduced axial ratio (c/a) and compressed Eu-layer space distance should play important roles. Interestingly, the calculations unveil that the out-of-plane FM structure hosts only one pair of Weyl nodes around the Fermi level, suggesting that pressure can be an alternative way to realize the ideal Weyl semimetal state in $EuCd_2As_2$ and will be useful for exploring exotic topological properties in such layered magnetic topological phase with strongly competing magnetic exchanges.

1. Introduction

Magnetic topological phases have arrested rapid growing research interest in recent years, because the interplay between magnetism and nontrivial topological band structure can produce extraordinary topological states such as the quantum anomalous Hall (QAH) insulator,[1,2] axion insulator,[3,4] and magnetic Weyl semimetal (WSM).[5–9] Generally, in a Dirac semimetal (DSM), the gapless crossing of two doubly degenerate bands forms the Dirac point (DP), which is protected by the combination of both inversion (P) and time-reversal (T) symmetries.[10,11] Once P or/and T can be broken, the twofold band degeneracy will be lifted and the crossings of nondegenerate bands then lead to Weyl points (WPs) that always appear in pairs with inverse spin chirality.[12,13] In a magnetic topological phase, the coupling between the spin and charge degrees of freedom offers opportunities to control different topological phases by magnetism, which enables the creation of ideal Weyl state through precisely manipulating the spin structure,

Z. Yu, W. Xia, Y. Guo
School of Physical Science and Technology
ShanghaiTech University
Shanghai 201210, China
E-mail: guoyf@shanghaitech.edu.cn

Z. Yu, M. Li, S. Li, X. Li, L. Wang
Center for High Pressure Science and Technology Advanced Research
Shanghai 201203, China
E-mail: inwang@ysu.edu.cn

The ORCID identification number(s) for the author(s) of this article can be found under https://doi.org/10.1002/qute.202200128

DOI: 10.1002/qute.202200128

Z. Yu, L. Wang
Center for High Pressure Science (CHiPS)
State Key Laboratory of Metastable Materials Science and Technology
Yanshan University
Qinhuangdao 066004, China

X. Chen, X. Lv, Z. Zhong
CAS Key Laboratory of Magnetic Materials and Devices & Zhejiang Province Key Laboratory of Magnetic Materials and Application Technology
Ningbo Institute of Materials Technology and Engineering
Chinese Academy of Sciences
Ningbo 315201, China
E-mail: zhong@nimte.ac.cn

W. Xia, Y. Guo
ShanghaiTech Laboratory for Topological Physics
ShanghaiTech University
Shanghai 201210, China

resembling the cases in the van der Waals antiferromagnetic (AFM) topological insulators (TIs) $MnBi_2Te_4/(Bi_2Te_3)_n$[3,4] and $MnSb_2Te_4/(Sb_2Te_3)_n$ ($n = 1, 2$).[8,9,14] These materials share similarities of strong spin–orbit coupling (SOC), low structural symmetry and long-range magnetic order, in which the spin rotation or polarization by external magnetic field can significantly alter the electronic band structure by the energy of even orders of magnitude larger than the traditional Zeeman splitting.[15]

The layered triangular lattice antiferromagnets $EuCd_2Pn_2$ (Pn = As, Sb) have captured considerable interest in recent years due to the WSM state in the spin-polarized structure.[6,7,16–20] $EuCd_2As_2$ is an itinerant magnet with conduction electrons from the Cd and As orbitals, and the magnetism originates from the local Eu 4*f* moments which form a long-range AFM order at $T_N \approx 9.5$ K with an A-type structure, i.e., ferromagnetic (FM) *ab* planes with in-plane lying spins stacking antiferromagnetically along the *c*-axis.[16] Such A-type AFM_in structure breaks the C_3 symmetry and consequently gaps the DP.[6,7] Compared with the large gap of ≈200 meV in $MnBi_2Te_4$, the small gap of only about tens meV in $EuCd_2As_2$ requires smaller energy to be closed, thus enabling the realization of FM WSM state with polarizing the spins along a specific direction, for example, the *c*-axis, by a moderate external magnetic field. Interestingly, an ideal WSM state in the *c*-axis direction spin-polarized structure was suggested with a single pair of WPs close to the G point along the G–A direction of the Brillouin zone, in a small window of energy free of other bands, thus providing a rare clean platform for the study of Weyl physics.[7]

Pressure is known to be a powerful and clean approach to tune crystallographic symmetry as well as electronic states for topological materials.[21,22] The WSM TaAs shows a phase transition from ambient pressure $I4_1md$ structure to a high pressure hexagonal *P*-6*m*2 structure at 14 GPa, with the number of WPs changing from 24 to 12.[23] Pressure-induced concurrence of superconductivity and topological phase transition was recently observed in the topological nodal-line semimetal $SrAs_3$.[24] Besides the nonmagnetic topological materials, high pressure was also verified as a productive means to tune the physical properties of magnetic topological materials.[25,26] For example, the out-of-plane FM order in the magnetic WSM $Co_3Sn_2S_2$ is suppressed by pressure, whereas in-plane AFM component is developed,[27] indicating that the magnetic structure could be manipulated by external pressure. Here, combining magnetization, magneto-transport and structure measurements under high pressure and first principles calculations, we find that application of pressure is capable of driving the in-plane AFM state across an intermediate in-plane FM state then into the out-of-plane FM state without structural phase transition and chemical valence change of Eu ions. The theoretical calculations indicate an ideal Weyl state will appear in the out-of-plane FM structure.

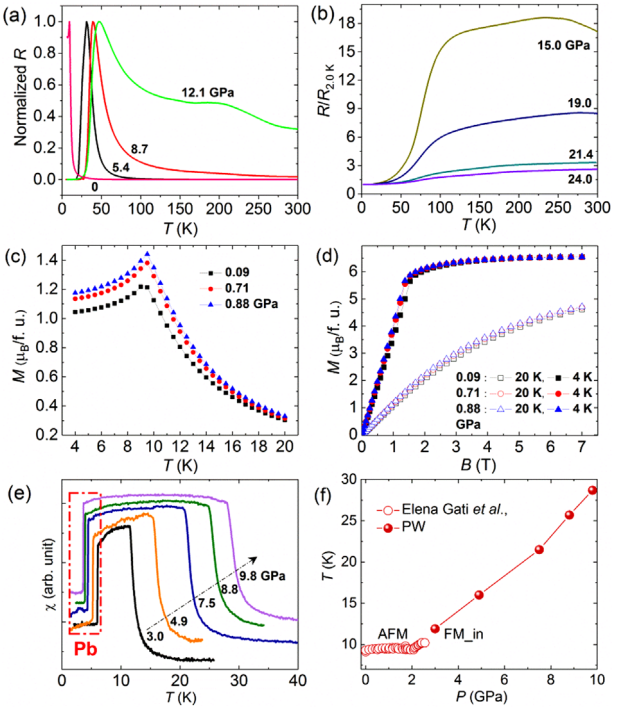

Figure 1. a,b) Temperature-dependent resistance of $EuCd_2As_2$ under various pressures. c) Temperature-dependent magnetizations under pressures lower than 0.9 GPa. d) Isothermal magnetizations at 4 and 20 K under pressures lower than 0.9 GPa. e) Temperature dependence of ac susceptibility for $EuCd_2As_2$ under selected pressures up to 9.8 GPa, where a remarkable magnetic phase transition from paramagnetic to ferromagnetic state is observed. The low temperature panel marked with rectangle is the diamagnetism from pressure calibrator of superconducting Pb. f) Pressure dependence of magnetic ordering temperature (T_N and T_C) of $EuCd_2As_2$. The open and solid symbols are the data from ref. [28] and present work, respectively.

2. Results and Discussion

The basic characterization results of $EuCd_2As_2$ crystals are presented in Figure S1a–f (Supporting Information). The temperature dependent resistance $R(T)$ of $EuCd_2As_2$ crystal measured at various pressures ranging from 0 to 24 GPa is presented in **Figure 1**a,b. The $R(T)$ at ambient pressure displays a sharp peak at ≈9.5 K signifying the AFM order. The measurements at pressure lower than 2.5 GPa was recently reported,[28] which shows that the AFM order could be slightly enhanced with increasing the pressure to 1.3 GPa, while the continuous increase of pressure larger than 1.3 GPa, on the contrary, can suppress the peak

N. Wang, D. Wu, W. Wu, Z. Liu, J. Luo, J. Cheng
Beijing National Lab for Condensed Matter Physics
Institute of Physics
Chinese Academy of Sciences
Beijing 100190, China

J. Zhao
School of Physics
Harbin Institute of Technology
Harbin 150080, China

Z. Dong, C. Zhou, L. Zhang
Shanghai Synchrotron Radiation Facility
Shanghai Advanced Research Institute
Chinese Academy of Sciences
Shanghai 201204, China

X. Wang, N. Yu, Z. Zou
Analytical Instrumentation Center
School of Physical Science and Technology
ShanghaiTech University
Shanghai 201210, China

to low temperature until the pressure reaches ≈2 GPa, which then rapidly pushes the peak to high temperature again. The behavior was ascribed to a spin transition from the AFM_in to FM_in configuration at ≈2 GPa. Our magnetic susceptibility and isothermal magnetizations measured below 0.9 GPa presented in Figure 1c,d support that the AFM order could be initially enhanced by pressure. We mainly focused on the characterizations on $EuCd_2As_2$ under pressure larger than 2.5 GPa that had not been measured yet. Seen in Figure 1a,b, with increasing pressure larger than 2.5 GPa, the peak signifying the FM_in order gradually shifts to high temperature, which becomes more and more broad and is eventually smeared out at pressure larger than 19.7 GPa. The $R(T)$ then displays a semimetallic conducting behavior over the measured temperature range.

To experimentally check the possibility of pressure-induced magnetic phase transition in $EuCd_2As_2$ suggested from the density functional theory (DFT) calculations presented later, the ac susceptibility measurement of $EuCd_2As_2$ was performed up to 9.8 GPa. Figure 1e shows the temperature dependence of ac susceptibility of $EuCd_2As_2$ under selected pressures up to 9.8 GPa, where a sharp enhancement of susceptibility intensity is observed, indicating a magnetic phase transition from PM to FM. The low temperature panel marked with rectangle is the diamagnetism from pressure calibrator of superconducting Pb. The magnetic ordering temperatures (T_N and T_C) as a function of pressure are shown in Figure 1f. The open and solid symbols are the data taken from ref. [28] and present work, respectively. It can be seen from Figure 1f that the T_N is not sensitive to applied pressure, while the T_C shows rapid increase as the pressure increases with a rate of ≈2.5 K GPa^{-1}. Moreover, the pressure induced T_C increase does not reach saturation up to 9.8 GPa. Here, the experimental observation of pressure-induced magnetic phase transition (AFM_in → FM_in) in $EuCd_2As_2$ is consistent with the present theoretical simulation results. Due to the limitation of high pressure magnetization measurements, the measurements in the present technique could not directly be performed up to the critical pressure (≈20 GPa) to confirm the theoretically suggested FM_in → FM_out transition as presented later. Furthermore, performing high pressure neutron diffraction experiment at ≈20 GPa is challenging for samples containing Eu element. Therefore, the magnetic state of FM_out of $EuCd_2As_2$ was determined relying on the DFT simulations.

Now we turn to investigate the evolution of magnetotransport of $EuCd_2As_2$ under high pressure. We noticed that $EuCd_2As_2$ exhibits negative MR (n-MR) under the pressures range of 20.8–31.1 GPa and at 2 K, seen in **Figure 2**a. In addition, a remarkable butterfly-shaped MR is observed with increasing the pressure. To achieve more insights into the extraordinary behavior of MR under high pressure, the temperature dependence of MR at 31.1 GPa was measured and is shown in Figure 2b. It is apparently that the butterfly-shaped hysteresis loop in the MR curve is suppressed as the temperature increases. The butterfly-shaped MR can persist even up to 50 K seen by the enlarged view as the inset of Figure 2b. So far as we know, the observation of butterfly-shaped MR in $EuCd_2As_2$ has not been reported yet, which while was ever reported in other ferromagnets such as Fe_3O_4[29] and Fe_5GeTe_2,[30] likely a further support of the FM state in $EuCd_2As_2$. Furthermore, a quasi-linear MR versus magnetic field is observed at 100 K. Unfortunately, since it is hard to perform crystallographic direction dependent n-MR measurements under very high pressure, we were unable to carry out further characterizations and hence the analysis to achieve in-depth insights into the underlying physics of the MR.

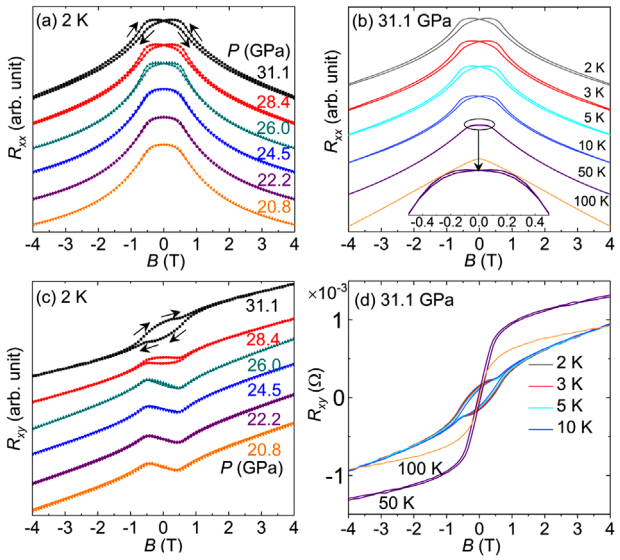

Figure 2. a) Pressure-dependent MR of $EuCd_2As_2$ at 2 K. The arrows mark the direction of magnetic field variation. b) MR under 31.1 GPa as a function of temperature. The inset shows the magnetic hysteresis within the magnetic field range of ±0.5 T at 50 K. c) Pressure-dependent Hall resistance of $EuCd_2As_2$ at 2 K. d) Temperature-dependent Hall resistance under 31.1 GPa.

The Hall resistance of $EuCd_2As_2$ at 2 K and under various pressures is shown in Figure 2c. Anomalous Hall effect (AHE) is displayed in the measured pressure range. Interestingly, a remarkable hysteresis loop in the Hall resistance under low magnetic field in the range of ±1.0 T is observed with increasing the pressure. Furthermore, the area of the hysteresis loop is apparently expanded with increasing the pressure. Figure 2d shows the temperature dependence of Hall resistance under 31.1 GPa. The hysteresis loops are only observed in the temperature range of 2–10 K and then are suppressed as the temperature increases. Since it is difficult to determine the magnetization of the sample under high pressure, we can only show the overall variation of the Hall resistance. We argue that the variation of the Hall resistance of $EuCd_2As_2$ under high pressure is correlated with the pressure-induced magnetic phase transition.

To examine the possibility of pressure-induced structural transition that is responsible for the variations of MR, Hall resistance and the magnetic phase transition, the structure evolution of $EuCd_2As_2$ under pressure were measured, with more details shown in the Supporting Information. Under ambient pressure, the Eu, Cd, and As atoms in $EuCd_2As_2$ are located at 1*a* (0, 0, 0), 2*d* (1/3, 2/3, 0.633), and 2*d* (1/3, 2/3, 0.247) Wyckoff positions, respectively. The $CdAs_4$ tetrahedra are slightly elongated with Cd-As distances ranging from 2.72 to 2.84 Å. The XRD patterns below 27.1 GPa could be well indexed on the basis of the $CaAl_2Si_2$-type structure (*P*-3*m*1), seen in Figure S2a (Supporting Information). The typical Rietveld refinement results of the AD-XRD patterns of $EuCd_2As_2$ collected at 0.7 and 23.8 GP (Run #1),

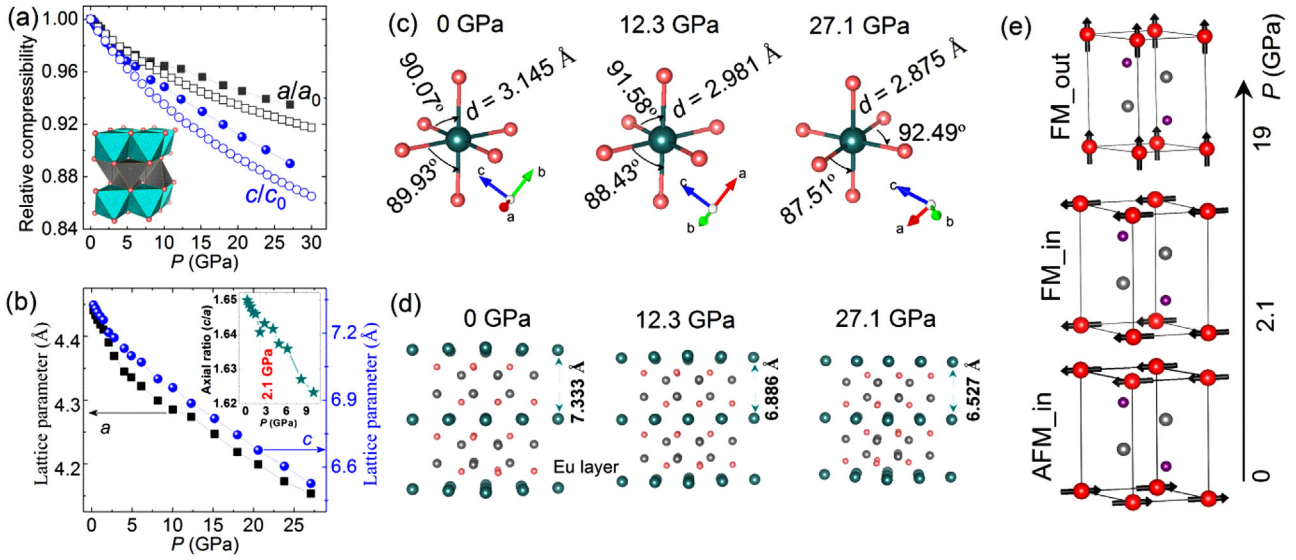

Figure 3. a) Pressure dependence of the relative compressibility a/a_0 and c/c_0 of $EuCd_2As_2$. The solid and open symbols correspond to experimental and calculated values, respectively. The inset shows the stacking of $EuAs_6$ octahedra and $CdAs_4$ tetrahedra in $EuCd_2As_2$. b) Pressure dependence of lattice parameter a and c. The inset shows the axial ratio c/a as a function of pressure. A remarkable inflection point is observed at 2.1 GPa. c) The pressure dependence of Eu—As bond length and ∠As—Eu—As bond angle, from which the pressure-induced $EuAs_6$ octahedron distortion is observed. d) The crystal structure of $EuCd_2As_2$ could be viewed as stacking of the Eu and CdAs layers along the c axis. The distance between two Eu interlayers is shrunk as the pressure increases, which gives rise to the variation of magnetic interaction. e) The present simulated magnetic phase transition in the sequential order of AFM_in → FM_in → FM_out under high pressure, in which the magnetic moment of Eu^{2+} is denoted by black arrows.

and 30.6 GPa (Run #2) are presented in Figure S3a–c (Supporting Information). When the pressure is larger than 35.5 GPa, new diffraction peaks signifying the emergence of new phases appear and the intensity of these peaks increase with further increasing the pressure, seen in Figure S2b (Supporting Information). However, the major phase of the sample is still the parent *P*-3*m*1 even up to 50.0 GPa. Unfortunately, it suffers a big difficulty for refining the new peaks due to the mixture with the *P*-3*m*1 phase and the peaks are too broad. The XRD patterns for the high-pressure phase of $EuCd_2As_2$ were shown in Figure S4 (Supporting Information). Interestingly, the parent phase could be recovered when the pressure was released to ambient pressure, seen in Figure S2b (Supporting Information).

According to the molecular field theory,[31] the magnetic ordering temperature (T_f) of a magnet is closely related with the effective exchange integral (J) between the magnetic ions. Provided that only the spin moment contributes to the magnetism within the nearest-neighbor interaction approximation, the T_f could be expressed as $k_B T_f = 2zS(S+1)J/3$, where k_B is Boltzmann constant, z is nearest atoms number, and S is spin quantum number, which shows that T_f is proportional to J. When the atomic distance is changed under certain conditions such as the application of external high pressure, J and hence the T_f will accordingly be varied. To trace the pressure-induced magnetic phase transitions in $EuCd_2As_2$, relative compressibility (a/a_0 and c/c_0) and the lattice parameters (a, c and axial ratio c/a) are plotted in **Figure 3**a,b, respectively. The *P*-3*m*1 phase is a layered structure with weak chemical bonding along the *c*-axis, and the *c*-axis is therefore more compressible than the *a*-axis, as shown in Figure 3a. The calculated lattice parameters summarized in Figure 3a agree well with the experimental ones. The pressure dependence of axial ratio c/a is shown by the inset of Figure 3b. The general tendency of c/a versus pressure exhibits a decrease with increasing pressure, which favors the competition between the AFM_in and FM_in magnetic phases. However, it is clearly visible that there is an inflection point around 2.1 GPa, which apparently signifies the magnetic phase transition from the AFM_in into the FM_in structure since the magnetic state is closely related with the evolution of crystal structure.

The *P*-3*m*1 crystal structure of $EuCd_2As_2$ could be visualized as a stacking of $EuAs_6$ octahedra and $CdAs_4$ tetrahedra along the *c* axis, as illustrated in inset of Figure 3a. The $EuAs_6$ octahedra are connected with each other through edge-sharing rather than apex-sharing. Figure 3c shows the pressure dependence of both Eu-As bond length and ∠As—Eu—As bond angle, which are labeled by their values. The pressure-induced $EuAs_6$ octahedron distortion between 0 and 27.1 GPa is observed, manifested by the change of ∠As—Eu—As from 90.07° to 92.49° and from 89.93° to 87.51°, respectively, as marked in Figure 3c. The Eu—As bond length is compressed about 8.58% as the pressure increases from 0 to 27.1 GPa. The distance between two Eu interlayers is shrunk from 7.333 to 6.527 Å, which is shortened by ≈11.0% and consequently gives rise to the variation of magnetic interaction, as illustrated in Figure 3d. As shown in Figure 3a, the relative compressibility of c/c_0 is larger than a/a_0 and their difference becomes more remarkable with increasing pressure. Such crystallographic environment favors the formation of FM_out state rather than FM_in state in $EuCd_2As_2$ when the pressure is larger than 20 GPa. The intra- and inter-layer Eu-Eu ions distances were ever found to have close correlations with the magnetic ordering temperature for a set of isostructural EuM_2X_2 (M = metal, X = pnictide) magnets.[32] Moreover, we investigated the magnetic phase transition of $EuCd_2As_2$ under high pressure by employing the first principles calculations. The simulated magnetic phase

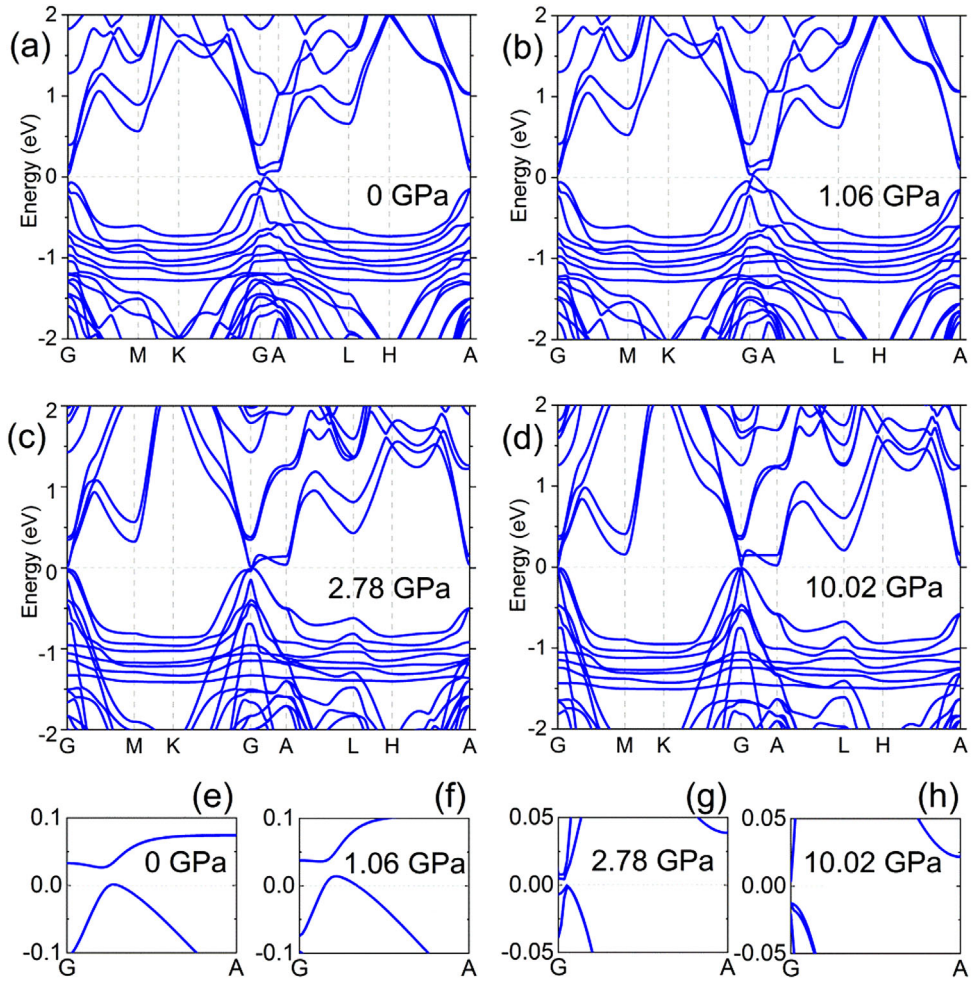

Figure 4. Band structures of the AFM_in magnetic state at a) ambient pressure and b) 1.06 GPa, respectively. The electronic band structures of the FM_in magnetic state at c) 2.78 GPa and d) 10.02 GPa. The band structures for those at low pressure are enlarged in (e)–(h) to show the variation of the bandgap.

transition in the sequential order of AFM_in → FM_in → FM_out under high pressure is shown in Figure 3e, in which the magnetic moment of Eu^{2+} is denoted with black arrows.

The possible variation of Eu^{2+} ($S = 7/2$, ≈7.0 μ_B) in $EuCd_2As_2$ under pressure was also examined by measuring the high pressure XANES spectra, seen by more details in the SI. The measured Eu L_1-edge XANES spectra of $EuCd_2As_2$ under various pressures are presented in Figure S5 (Supporting Information). It was shown that the absorption energy of the Eu L_1-edge shifts towards higher energy as the pressure increases. For a convenient comparison, the Eu L_1-edge XANES data of EuS with Eu^{2+} and Eu_2O_3 with Eu^{3+} are also plotted together. As shown in Figure S5 (Supporting Information), the linewidth of Eu L_1-edge becomes broader upon the increase of pressure, which might be resulted from the enhanced Eu(4*f*)-As(4*p*) hybridization or/and the intermediate valence states of Eu ions under pressure.[33] The XANES spectra for $EuCd_2As_2$, EuS, and Eu_2O_3 clearly demonstrate that the L_1-edge energy shifts depending on the oxidation state of Eu ions.[34] It is notable that the pre-edge peak labeled as PE remains nearly unchanged while the WL peak slightly shifts to higher photon energy with the increase of pressure. A quantitative analysis of the oxidation state of Eu in $EuCd_2As_2$ under high pressure (see Table S1, Supporting Information) was performed by using the same method reported in reference.[34] The valence of Eu ions in $EuCd_2As_2$ at ≈20.0 GPa exhibits intermediate state of ~ +2.07. The peak positions of $EuCd_2As_2$ during compression and decompression to ambient pressure (marked as "D" in Figure S5, Supporting Information) are almost the same, indicating that the pressure-induced transition of +2 to intermediate valence at high pressure is reversible.

The recent theoretical studies indicated gate/strain tunable topological phase transition of $EuCd_2As_2$.[35,36] Here, the first principles calculations were performed to investigate the magnetic phase transitions and the possible associated evolution of electronic band structure topology in $EuCd_2As_2$ under high pressure. The calculations were carried out with considering several possible magnetic structure models and variable Hubbard *U* energy values. The theoretical calculation results suggest that the ferromagnetic state of $EuCd_2As_2$ with Eu spins along the *c*-axis is the most stable one under ≈20 GPa. **Figure 4**a,b shows the band structures of $EuCd_2As_2$ at ambient pressure and 1.06 GPa with the AFM_in structure. At ambient pressure, a small gap about

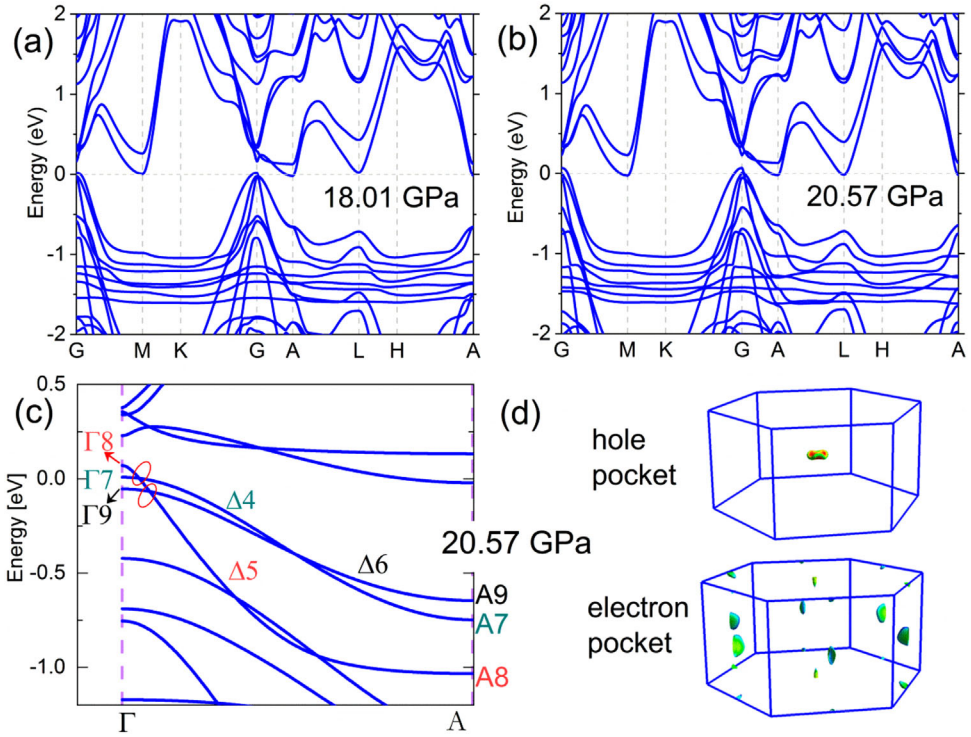

Figure 5. a) The electronic band structure of the FM_in magnetic state at 18.01 GPa and that for the FM_out magnetic state at b) 20.57 GPa. c,d) The band structure and Fermi surface of $EuCd_2As_2$ at 20.57 GPa, respectively. Two pairs of WPS could be recognized along the G-A high symmetry line of the Brillouin zone.

0.025 eV at the G point of the Brillouin zone could be recognized, seen by the enlarged view in Figure 4e, which slightly decreases to 0.022 eV at 1.06 GPa, seen by the enlarged view in Figure 4f. The gap is still visible even in the FM_in structure, seen by the enlarged views in Figure 4g,h taken from the band structures in Figure 4c,d calculated at 2.78 and 10.02 GPa, respectively. However, with further increase of pressure, the gap is gradually closed with both electron- and hole-type bands crossing the E_F, seen in **Figure 5**a,b with the pressure of 18.01 and 20.57 GPa, respectively. The electron and hole pockets of the Fermi surface under 20.57 GPa are illustrated in Figure 5d. When the pressure is lower than 18.01 GPa, the total energy calculations suggest that the FM_in state is the most stable one as compared with the other two magnetic configurations. It is clear that the band structures of the FM_in state show clear band inversion at the G point, seen in both Figure 4c,d.

Figure S6 (Supporting Information) shows the calculated magnetic ground states of $EuCd_2As_2$ at different Hubbard U values and external pressures. The magnetic ground state of $EuCd_2As_2$ is closely related with the U values as well as the external pressure. When the Hubbard U values are larger than 3 eV, the AFM_in structure is the most stable at ambient pressure. If U is smaller than 3 eV, the magnetic ground state is always with the FM_out structure regardless of the external pressure, thus exposing the crucial role of the on-site Coulomb interaction. In order to match the normalized lattice constants variation, here U is set as 4 eV. With gradual increase of pressure from 2.1 to 19 GPa, the magnetic ground state experiences the AFM_in, FM_in and finally enters into the FM_out structure. This phase presents magnetic space group $P\text{-}3m'1$ (164.89 BNS setting) with breaking T and retaining P. The high pressure apparently favors the FM_out structure that can realize the Weyl state, which is tested by Weyl chirality calculation and magnetic topological quantum chemistry (MTQC). As is illustrated in Figure 5c, linear band crossing points could be well recognized along the G-A high symmetry line, with only two crossing points at the position (0.000, 0.000, $\pm$0.0383 Å^{-1}) and (0.000, 0.000, $\pm$0.0581 Å^{-1}) which are rather close to E_F. The chirality analysis suggests the crossing points are WPs, thus the Weyl state could be regarded as an ideal Weyl state protected by P. At the same time, these results are also verified by calculations based on MTQC, which support enforced semimetal along G-A high symmetry line. As shown in Figure 5c, the compatibility relations at the three highest valance bands support these two symmetry-protected linear crossing points due to the exchange order of irreducible co-representation at high symmetry points G and A. Apart from these points, there might be a symmetry protected or accidental crossing point with energy position away from E_F, which is less concerned. Furthermore, the modified Becke–Johnson method was performed to calculate the Weyl chirality, which gives the same result as that derived from the DFT+U method. The magnetic ground states and band structures of $EuCd_2As_2$ (Table S2 and Figure S7, Supporting Information) were also performed by using the HSE method, with the results being fully consistent with the present results.

To summarize, the application of pressure is capable of driving the layered topological semimetal $EuCd_2As_2$ into sequential magnetic states with increasing the pressure, including the AFM_in, FM_in and FM_out structures, with changing neither

the $CaAl_2Si_2$-type crystal structure nor the Eu^{2+} valence state. The analysis of the crystal structure under pressure indicates that the evolutions of the axial ratio (c/a) and Eu-layer distance play important roles in driving the magnetic phase transition. The magnetic phase transitions are supported by the high pressure magnetism measurement and first principles calculations. Coupled with the pressure-induced magnetic phase transition, butterfly-shaped MR and anomalous Hall effect are observed. Interestingly, in the FM_out structure, the calculations unveil only one pair of Weyl points near the Fermi level, which could be regarded as an ideal Weyl state. This work indicates that external pressure can also realize the ideal Weyl state that ever produced by the application of external magnetic field on $EuCd_2As_2$, which however still need to be verified by straightforward detection techniques. The result would be instructive for the discovery of more novel exotic topological properties in magnetic topological phases by using high pressure.

3. Experimental and Calculation Details

3.1. Single Crystal Growth and Basic Characterizations

The $EuCd_2As_2$ single crystals were grown by using a Sn flux method with the procedure similar as that in a reported reference.[7] The picture for plate-like black crystal with shining surface and a typical size of $1 \times 1 \times 0.2$ mm^3 is shown in Figure S1a (Supporting Information). The crystal quality was examined on a Bruker D8 single crystal X-ray diffractometer with $\lambda = 0.71073$ Å at room temperature. The obtained lattice parameters are $a = 4.4423$ Å and $c = 7.333$ Å, which are consistent with those reported reference.[7] The clean reciprocal diffraction patterns shown in Figure S1b–d (Supporting Information) without other impurity spots indicate the high quality of our single crystals. The schematic crystal and magnetic structures of $EuCd_2As_2$ was shown in Figure S1e (Supporting Information). Temperature dependence of the magnetic susceptibility of $EuCd_2As_2$ measured in an external field of 1000 Oe was shown in Figure S1f (Supporting Information).

3.2. Magnetic Properties Measurement under Ambient and High Pressure

The direct current magnetization (M) for $EuCd_2As_2$ was measured in a Quantum Design magnetic property measurement system (MPMS). The Néel temperature T_N of ≈9.5 K derived from the M–T data, as shown in Figure S1f (Supporting Information), was consistent with the previously reported value.[7] The magnetizations measurements under high pressure were performed using a miniature BeCu piston-cylinder cell measured on a commercial magnetic property measurement system from Quantum Design. The $EuCd_2As_2$ single crystals together with a piece of Sn were loaded into a Teflon capsule filled with Daphne 7373 as the pressure transmitting medium (PTM). Pressure at low temperatures was determined from the shift of the superconducting transition temperature of elemental Sn. All of the magnetization curves are measured in the zero-field-cooling mode.

The ac susceptibility for $EuCd_2As_2$ single crystals was measured by using a palm-type cubic anvil cell (CAC) under various hydrostatic pressures up to 9.8 GPa.[37] Here, we used glycerol as the liquid PTM in CAC. The ac susceptibility of $EuCd_2As_2$ together with a piece of Pb placed in the same coil was measured with the mutual induction method. An excitation current of ~ 1 mA with a frequency of 1117 Hz was applied to the primary coil and the output signal was picked up with a Stanford Research SR830 lock-in amplifier. The measured superconducting transition of Pb was used to determine the pressure value in CAC.

3.3. High-Pressure and Low-Temperature Electrical/Magnetic Transport Measurement

A symmetric diamond anvil cell (DAC) with an anvil culet of 400 μm in diameter was utilized to generate high pressure. A four-probe method by using Pt as the electrodes was used for in situ electrical resistance measurements under pressure. The magnetoresistance (MR) and Hall effect measurement under pressure was performed between 2 and 100 K. The manufacturing process of the microcircuit was similar to that described in our previous work.[38] The PTM was not used for the resistance measurement. A ruby ball was used as the pressure calibrator.[39]

3.4. High-Pressure Angle Dispersive X-Ray Diffraction (AD-XRD) and X-Ray Absorption Spectroscopy (XAS)

The $EuCd_2As_2$ crystals were ground in a mortar in order to obtain fine powder sample that is used for high pressure AD-XRD and X-ray absorption near-edge spectroscopy (XANES) measurements. The high pressure AD-XRD measurement was carried out using a symmetric DAC. The AD-XRD patterns were taken with a MarCCD detector using synchrotron radiation beams monochromatized to a wavelength of 0.6199 Å at the beamline BL15U1 of Shanghai Synchrotron Radiation Facility (SSRF). Run #1 was performed at BL15U1 with silicone oil as PTM up to 27.1 GPa. Another independent Run #2 AD-XRD measurement up to 50.0 GPa was carried out at the beamline of 16-ID-B ($\lambda = 0.4066$ Å) at the Advanced Photon Source (APS) of Argonne National Laboratory. The 2D image plate patterns were converted into the one-dimension intensity versus degree data by using the Fit2D software package.[40] The experimental pressures were determined by the pressure-induced fluorescence shift of ruby.[39] The XRD patterns were analyzed with Rietveld refinement using the GSAS program package[41] with a user interface EXPGUI.[42]

High-pressure XANES experiments at Eu L_1-edge were performed at beamline 20-BM-B at APS of ANl. The XAS measurements were performed in the transmission mode. The incident beam was monochromatized with two Si (111) single crystals. Silicone oil was used as the PTM. The sample pressure was determined using the standard ruby fluorescence technique.[39] To reduce the absorption from the diamond anvils, nanopolycrystal diamond was used. The chemical valence of Eu in EuS (+2) and Eu_2O_3 (+3)[43] was selected as the reference for detecting the valence variation of Eu in $EuCd_2As_2$ under high pressure.

3.5. The Ab Initio Calculations

Pressured-induced structural and electronic properties of $EuCd_2As_2$ were simulated with the projector augmented wave

method[44] and Perdew–Burke–Ernzerhof revised for solids (PBEsol)[45] scheme based on Vienna Ab initio simulation package (VASP).[46] The Brillouin zone was sampled with $12 \times 12 \times 4$ (AFM) and $12 \times 12 \times 8$ (FM) Monkhorst–Pack *k*-mesh and kinetic energy cutoff was set to 500 eV. Experimental lattice parameters were used for calculating the magnetic ground states at the different pressures with setting the on-site Coulomb interactions of Eu 4*f* electrons from 0 to 6 eV. The spin–orbit coupling was included for a self-consistence. Eu 4*f*5*d*, Cd 5*s*, and As 4*p* orbitals were projected onto maximally localized Wannier functions based on VASP2WANNIER interface.[47] This projected process was also performed with modified Becke–Johnson method.[48] Corresponding topological properties were calculated with WANNIERTOOLS[49] and the Fermi surface was plotted by FermiSurfer.[50] MTQC method was also used to calculate the compatibility relations by using MagVasp2trace package.[51–53]

Supporting Information

Supporting Information is available from the Wiley Online Library or from the author.

Acknowledgements

Z.H.Y. and X.J.C. contributed equally to this work. The authors acknowledge the support by the National Natural Science Foundation of China (Grant Nos. 92065201, 12134018, 12025408, and 11921004) and the Shanghai Science and Technology Innovation Action Plan (Grant No. 21JC1402000). Y.F.G. acknowledges the open projects from Beijing National Laboratory for Condensed Matter Physics (Grant No. ZBJ2106110017) and State Key Laboratory of Functional Materials for Informatics (Grant No. SKL2022). Z.C.Z. was supported by Science Center of the National Science Foundation of China (52088101). J.G.C. was supported by the National Key R&D Program of China (2018YFA0305700) and Beijing Natural Science Foundation (Z190008). The high-pressure experiments with cubic anvil cell were performed at the Synergic Extreme Condition User Facility (SECUF). Part of the experiments was performed at the BL15U1 beamline of Shanghai Synchrotron Radiation Facility (SSRF) in China, and the 16 ID-B, Advanced Photon Source (APS) of Argonne National Laboratory (ANL). The synchrotron X-ray absorption spectrum was performed at 20 BM-B of APS at ANL. The authors thank Steve. M. Heald and colleagues for help with experiment. The authors also thank the support from the Double First-Class Initiative Fund of ShanghaiTech University and the Analytical Instrumentation Center (Grant No. SPST-AIC10112914), SPST, ShanghaiTech University.

Conflict of Interest

The authors declare no conflict of interest.

Data Availability Statement

The data that support the findings of this study are available from the corresponding author upon reasonable request.

Keywords

crystal structure, high pressure, magnetic topological phase, magneto-transport, Weyl semimetal

Received: September 29, 2022
Revised: February 27, 2023
Published online: March 22, 2023

[1] T. Suzuki, L. Savary, J.-P. Liu, J. W. Lynn, L. Balents, J. G. Checkelsky, *Science* **2019**, *365*, 377.
[2] J. P. Liu, L. Balents, *Phys. Rev. Lett.* **2017**, *119*, 087202.
[3] C. Hu, L. Ding, K. N. Gordon, B. Ghosh, H.-J. Tien, H. Li, A. G. Linn, S. W. Lien, D. L. Song, S.-Y. Xu, H. Lin, H. Cao, T.-R. Chang, D. Dessau, N. Ni, *Sci. Adv.* **2020**, *6*, eaba4275.
[4] M. M. Otrokov, I. P. Rusinov, M. Blanco-Rey, M. Hoffmann, A. Y. Vyazovskaya, S. V. Eremeev, A. Ernst, P. M. Echenique, A. Arnau, E. V. Chulkov, *Phys. Rev. Lett.* **2019**, *122*, 107202.
[5] Y. Deng, Y. Yu, M. Z. Shi, Z. Guo, Z. Xu, J. Wang, X. H. Chen, Y. Zhang, *Science* **2020**, *367*, 895.
[6] H. Su, B. C. Gong, W. J. Shi, H. F. Yang, H. Y. Wang, W. Xia, Z. Y. Yu, P. J. Guo, J. H. Wang, L. C. Ding, L. C. Xu, X. K. Li, X. Wang, Z. Q. Zou, N. Yu, Z. W. Zhu, Y. L. Chen, Z. K. Liu, K. Liu, G. Li, Y. F. Guo, *APL Mater.* **2020**, *8*, 011109.
[7] J. R. Soh, F. de Juan, M. G. Vergniory, N. B. M. Schröter, M. C. Rahn, D. Y. Yan, J. Jiang, M. Bristow, P. Reiss, J. N. Blandy, Y. F. Guo, Y. G. Shi, T. K. Kim, A. McCollam, S. H. Simon, Y. Chen, A. I. Coldea, A. T. Boothroyd, *Phys. Rev. B* **2019**, *100*, 201102.
[8] S. C. Huan, D. H. Wang, H. Su, H. Y. Wang, X. Wang, N. Yu, Z. Q. Zou, H. J. Zhang, Y. F. Guo, *Appl. Phys. Lett.* **2021**, *118*, 192105.
[9] S. C. Huan, S. H. Zhang, Z. C. Jiang, H. Su, H. Y. Wang, X. Zhang, Y. C. Yang, Z. T. Liu, X. Wang, N. Yu, Z. Q. Zou, D. W. Shen, J. P. Liu, Y. F. Guo, *Phys. Rev. Lett.* **2021**, *126*, 246601.
[10] Z. Wang, Y. Sun, X. - Q. Chen, C. Franchini, G. Xu, H. Weng, X. Dai, Z. Fang, *Phys. Rev. B* **2012**, *85*, 195320.
[11] Z. Wang, H. Weng, Q. Wu, X. Dai, Z. Fang, *Phys. Rev. B* **2013**, *88*, 125427.
[12] X. Wan, A. M. Turner, A. Vishwanath, S. Y. Savrasov, *Phys. Rev. B* **2011**, *83*, 205101.
[13] S.-Y. Xu, I. Belopolski, N. Alidoust, M. Neupane, G. Bian, C. L. Zhang, R. Sankar, G. Q. Chang, Z. J. Yuan, C.-C. Lee, S.-M. Huang, H. Zheng, J. Ma, D. S. Sanchez, B. K. Wang, A. Bansil, F. C. Chou, P. P. Shibayev, H. Lin, S. Jia, M. Z. Hasan, *Science* **2015**,*349*, 613.
[14] T. Murakami, Y. Nambu, T. Koretsune, G. Xiangyu, T. Yamamoto, C. M. Brown, H. Kageyama, *Phys. Rev. B* **2019**, *100*, 195103.
[15] Z. L. Liao, P. H. Jiang, Z. C. Zhong, R. W. Li, *npj Quantum Mater.* **2020**, *5*, 30.
[16] M. C. Rahn, J.-R. Soh, S. Francoua, L. S. I. Veiga, J. Strempfer, J. Mardegan, D. Y. Yan, Y. F. Guo, Y. G. Shi, A. T. Boothroyd, *Phys. Rev. B* **2018**, *97*, 214422.
[17] J.-Z. Ma, S. M. Nie, C. J. Yi, J. Jandke, T. Shang, M. Y. Yao, M. Naamneh, L. Q. Yan, Y. Sun, A. Chikina, V. N. Strocov, M. Medarde, M. Song, Y.-M. Xiong, G. Xu, W. Wulfhekel, J. Mesot, M. Reticcioli1, C. Franchini, C. Mudry, M. Müller, Y. G. Shi, T. Qian, H. Ding, M. Shi, *Sci. Adv.* **2019**, *5*, eaaw4718.
[18] N. H. Jo, B. Kuthanazhi, Y. Wu, E. Timmons, T. H. Kim, L. Zhou, L. L. Wang, B. G. Ueland, A. Palasyuk, D. H. Ryan, R. J. McQueeney, K. Lee, B. Schrunk, A. A. Burkov, R. Prozorov, S. L. Bud'ko, A. Kaminski, P. C. Canfield, *Phys. Rev. B* **2020**, *101*, 140402(R).
[19] L. L. Wang, N. H. Jo, B. Kuthanazhi, Y. Wu, R. J. McQueeney, A. Kaminski, P. C. Canfield, *Phys. Rev. B* **2019**, *99*, 245147.
[20] G. Hua, S. Nie, Z. Song, R. Yu, G. Xu, K. Yao, *Phys. Rev. B* **2018**, *98*, 201116.
[21] Z. H. Yu, L. Wang, Q. Y. Hu, J. G. Zhao, S. Yan, K. Yang, S. Sinogeikin, G. D. Gu, H. K. Mao, *Sci. Rep.* **2015**, *5*, 15939.
[22] M. T. Li, K. L. Xu, M. Xu, Y. F. Fang, Z. P. Yan, N. N. Li, Z. H. Yu, J. B. Zhang, C. Kenney-Benson, X. L. Wang, L. Wang, *Phys. Rev. B* **2019**, *100*, 224521.
[23] Y. H. Zhou, P. C. Lu, Y. P. Du, X. D. Zhu, G. H. Zhang, R. R. Zhang, D. X. Shao, X. L. Chen, X. F. Wang, M. L. Tian, J. Sun, X. G. Wan, Z. R. Yang, W. G. Yang, Y. H. Zhang, D. Y. Xing, *Phys. Rev. Lett.* **2016**, *117*, 146402.

[24] E. J. Cheng, W. Xia, X. B. Shi, Z. H. Yu, L. Wang, L. M. Yan, D. C. Peets, C. C. Zhu, H. Su, Y. Zhang, D. Z. Dai, X. Wang, Z. Q. Zou, N. Yu, X. F. Kou, W. G. Yang, W. W. Zhao, Y. F. Guo, S. Y. Li, *npj Quantum Mater.* **2020**, *5*, 38.
[25] Z. Y. Liu, T. Zhang, S. X. Xu, P. T. Yang, Q. Wang, H. C. Lei, Y. Sui, Y. Uwatoko, B. S. Wang, H. M. Weng, J. P. Sun, J.-G. Cheng, *Phys Rev* **2020**, *4*, 044203.
[26] T. Qian, E. Emmanouilidou, C. W. Hu, J. C. Green, I. I. Mazin, N. Ni, *Nano Lett.* **2022**, *22*, 5523.
[27] Q. Q. Zeng, H. Y. Sun, J. L. Shen, Q. S. Yao, Q. Zhang, N. N. Li, L. Jiao, H. X. Wei, C. Felser, Y. G. Wang, Q. H. Liu, E. K. Liu, *Adv. Quantum Technol.* **2022**, *5*, 2100149.
[28] E. Gati, S. L. Bud'ko, L. L. Wang, A. Valadkhani, R. Gupta, B. Kuthanazhi, L. Xiang, J. M. Wilde, A. Sapkota, Z. Guguchia, R. Khasanov, R. Valentí, P. C. Canfield, *Phys. Rev. B* **2021**, *104*, 155124.
[29] P. Li, L. T. Zhang, W. B. Mi, E. Y. Jiang, H. L. Bai, *J. Appl. Phys.* **2009**, *106*, 033908.
[30] T. Ohta, M. Tokuda, S. Iwakiri, K. Sakai, B. Driesen, Y. Okada, K. Kobayashi, Y. Niimi, *AIP Adv.* **2021**, *11*, 025014.
[31] J. S. Smart, *Effective Field Theories of Magnetism*, W. B. Saunders Co., Philadelphia, PA **1966**.
[32] T. Berry, V. J. Stewart, B. W. Y. Redemann, C. Lygouras, N. Varnava, D. Vanderbilt, T. M. McQueen, arXiv 2203.12739, **2022**.
[33] C. Y. Li, Z. H. Yu, W. L. Bi, J. Y. Zhao, M. Y. Hu, J. G. Zhao, W. Wu, J. L. Luo, H. Yan, E. E. Alp, H. Z. Liu, *Phys. B* **2016**, *501*, 101.
[34] T. Yamamoto, A. Yukumoto, *J. Anal. At. Spectrom.* **2018**, *33*, 585.
[35] C. W. Niu, N. Mao, X. T. Hu, B. B. Huang, Y. Dai, *Phys. Rev. B* **2019**, *99*, 235119.
[36] B. Y. Li, W. L. Sun, X. R. Zou, X. Y. Li, B. B. Huang, Y. Dai, C. W. Niu, *New J. Phys.* **2022**, *24*, 053038.
[37] J. G. Cheng, K. Matsubayashi, S. Nagasaki, A. Hisada, T. Hirayama, M. Hedo, H. Kagi, Y. Uwatoko, *Rev. Sci. Instrum.* **2014**, *85*, 093907.
[38] H. Y. Wang, C. Y. Pei, H. Su, Z. H. Yu, M. T. Li, W. Xia, X. L. Liu, Q. F. Liang, J. G. Zhao, C. Y. Zhou, N. Yu, X. Wang, Z. Q. Zou, L. Wang, Y. P. Qi, Y. F. Guo, *Appl. Phys. Lett.* **2019**, *115*, 122403.
[39] H. K. Mao, J. Xu, P. Bell, *J. Geophys. Res.* **1986**,*91*, 4673.
[40] A. Hammersley, S. Svensson, M. Hanfland, A. Fitch, D. Hausermann, *High Pressure Res.* **1996**, *14*, 235.
[41] A. C. Larson, R. B. Von Dreele, Los Alamos National Laboratory Report LAUR 86–748, **1994**.
[42] B. H. Toby, *J. Appl. Crystallogr.* **2001**, *34*, 210.
[43] H. Hayashi, Y. Takehara, N. Kawamura, M. Mizumaki, *Ana. Sci.* **2010**, *26*, 885.
[44] P. E. Blöchl, *Phys. Rev. B* **1994**, *50*, 17953.
[45] J. P. Perdew, A. Ruzsinszky, G. I. Csonka, O. A. Vydrov, G. E. Scuseria, L. A. Constantin, X. L. Zhou, K. Burke, *Phys. Rev. Lett.* **2008**, *100*, 136406.
[46] G. Kresse, J. Furthmüller, *Phys. Rev. B* **1996**, *54*, 11169.
[47] A. A. Mostofifi, J. R. Yates, G. Pizzi, Y.-S. Lee, I. Souza, D. Vanderbilt, N. Marzari, *Comput. Phys. Commun.* **2014**, *185*, 2309.
[48] F. Tran, P. Blaha, *Phys. Rev. Lett.* **2009**, *102*, 226401.
[49] Q. S. Wu, S. N. Zhang, H.-F. Song, M. Troyer, A. A. Soluyanov, *Comput. Phys. Commun.* **2018**, *224*, 405.
[50] M. Kawamura, *Comput. Phys. Commun.* **2019**,*239*, 197.
[51] L. Elcoro, B. J. Wieder, Z. D. Song, Y. F. Xu, B. Bradlyn, B. A. Bernevig, *Nat. Commun.* **2021**, *12*, 5965.
[52] Y. F. Xu, L. Elcoro, Z. D. Song, B. J. Wieder, M. G. Vergniory, N. Regnault, Y. L. Chen, C. Felser, B. A. Bernevig, *Nature* **2020**, *586*, 702.
[53] J. Kruthoff, J. de Boer, J. Van Wezel, C. L. Kane, R.-J. Slager, *Phys. Rev. X* **2017**, *7*, 041069.